*Int. J. Electrochem. Sci.*, 15 **(2020)** 6405 – 6424, doi: 10.20964/2020.07.68

**International Journal of**
**ELECTROCHEMICAL**
**SCIENCE**
www.electrochemsci.org

# Corrosion and Biocompatibility Behavior of the Micro-Arc Oxidized AZ31B Alloy in Simulated Body Fluid

*Chun-Ying Lee*[1], *Kun-Lin Chen*[1], *Zhu-Min Xu*[2], *and Hung-Bin Lee*[3,*]

[1] Graduate Institute of Manufacturing Technology, National Taipei University of Technology,
Taipei 10608, Taiwan
[2] Bachelor Program for Design and Materials for Medical Equipment and Devices, Da-Yeh University,
Changhua 515, Taiwan
[3] Department of Optoelectronics and Materials Technology, National Taiwan Ocean University,
Keelung 202, Taiwan
[*]E-mail: lhb6018@mail.ntou.edu.tw

*Received:* 16 March 2020 / *Accepted:* 11 May 2020 / *Published:* 10 June 2020

---

The corrosion behavior of AZ31B magnesium alloy in simulated body fluid (SBF) was investigated in this study. In order to improve its corrosion resistance, a micro-arc oxidation (MAO) treatment was performed on the AZ31B specimen. Specimens subjected to different processing durations in the electrolyte containing silicate, sodium hydroxide and sodium citrate were prepared with pulsed direct current first. The then measured potentio-dynamic polarization curve of the specimen in SBF revealed that the one with 30-min treatment had the best corrosion resistance. After submersion of the MAO specimen in SBF for several days, the microstructural examination on the cross-section showed the infusion of SBF through the porous and cracked oxide and induced corrosion near the substrate. At the same time, a homogeneous layer of apatite appeared on the surface of the specimen in the original porous oxide layer. This apatite layer was confirmed by the measured Ca/P molar ratio of 1.54-1.67 through its thickness. Moreover, the cell toxicity of this AZ31B specimen was tested using mouse neuroma cells. The cultivation of the cell in cytotoxicity test showed good survival rate and the axon was grown on the division of the cells.

---

**Keywords:** AZ31B, micro-arc oxidation, simulated body fluid (SBF), corrosion, cytotoxicity

## 1. INTRODUCTION

Magnesium and its alloys have known to possess similar elastic modulus, mechanical property and cell inductivity with human bones, which can minimize the stress shielding effect when they are used as implants in vivo [1-3]. The other advantageous effect of this type of implant is its potential biodegradability in vivo. More explicitly speaking, the implant inside the human tissue can start to degrade slowly with controllable and biocompatible fashion to provide temporal support and yet no surgical need to remove it after the tissue is fully recovered [1-10]. However, some researchers, such as Lambotte [4], Heublein et al. [5], Wittea et al. [6], reported the possible occurrence of too fast degradation of the magnesium alloy implants. Therefore, the topic in reducing the corrosion rate and yet maintaining the required mechanical property and biocompatibility of magnesium alloy implant poses an important challenge for its development [18-20].

It is known that magnesium and its alloys have low chemical stability, high electronegativity and activity in chemical reaction. Oxidation film forms easily at room temperature and atmospheric environment. However, this oxide film is prone to mechanical abrasion and facilitates continuous oxidation into the substrate. When the magnesium alloy is used in vivo, the environment with high concentration of chlorine ion causes its quick corrosion and local alkalization. Thus, the corrosion reaction promotes the cytotoxicity and impedes the rehabilitation of the tissues [12-16]. Erinc and coworkers [17] proposed the corrosion threshold of 0.5 mm/Y in order to maintain the biocompatibility of magnesium alloy. Because of the high chemical reactivity, the corrosion of magnesium alloy usually occurs locally. This local weakening in geometry increases the stress concentration and, subsequently facilitates the fracture in loading.

Since the magnesium alloy is prone to environmental attack, a surface modification will be an effective tool to improve its corrosion resistance, sustain its designed function, and raise its biocompatibility [21-23]. Among the proposed surface treatments, micro-arc oxidation (MAO) process prepares a porous oxide layer on the treated parts. This porous oxide layer not only increases the corrosion resistance but also provides the surface cavities for the cells to adhere and grow. Therefore, it can have good bonding with bone tissues and other beneficial functions such as higher corrosion and wear resistances, thermal stability and hardness [24-26]. Pan and coworkers [24] studied the corrosion polarization curves of Mg-alloys in trishydroxymethyl-aminomethane hydrochloric acid (Tris-HCl) buffer and simulated body fluid (SBF) solutions, respectively. They reported that the MAO-treated surface was better in degradability and bioactivity than its substrates (pure Mg, Mg-Ca and Mg-Ca-Zn alloys). Jian and coworkers [26] investigated the corrosion of LZ91 substrate and MAO-coated specimen in 3.5wt% NaCl solution. The pristine LZ91 substrate was found to have the lowest corrosion potential ($E_{corr}$), highest corrosion current ($I_{corr}$), and subsequently, fastest corrosion rate. The function of MAO treatment on improving the corrosion resistance of LZ91 was manifested. The MAO treatment of magnesium alloy can be controlled by several process parameters: material compositions, electrolyte bath, applied power (current, voltage and frequency), reaction time duration, and temperature [27]. Moreover, the corrosion resistance of the MAO treated surface can be further improved by additional coating from an organic sol-gel process. Toorani and coworkers [28] added $CeO_2$ nanoparticles into the electrolyte for MAO treatment and subsequently submerged the processed magnesium alloy into an organic bath of 70 wt% epoxy and 30 wt% polyamine to reduce the corrosion rate. Li and coworkers [29] submerged MAO processed AZ31 magnesium alloy into an alkaline bath containing ethylene diamine tetra-acetic acid disodium salt dehydrate (EDTA-2Na) to form compact $Mg(OH)_2$ coating and reduce the corrosion current effectively. Zheng et al. [30] post-processed the MAO coated surface with hydroxyapatite ($Ca_{10}(PO_4)_6(OH)_2$, HA） by using sol-gel method. The MAO surface and sol-gel coating had excellent bonding which greatly reduced the corrosion current and improved the biocompatibility.

The sealing post-treatment using submersion in aqueous solution with inorganic salts (cerium and stannate based salts) and organic salt (octodecylphosphate acid, $C_{18}H_{39}O_3P$, ODP) was reported by Mingo and coworkers [31] to improve the corrosion resistance.

Wang et al. [32] and Krishna et al. [33], respectively investigated the influence of alloying elements in the MAO treatment of magnesium alloy. The alloying elements of Al and Zn were found in favor of the growth rate of MAO coating. The addition of 6-9 wt% of Al was able to raise the coating's hardness and reduce the alloy's degradation rate. In terms of the electrolytes used in MAO treatment, most studies used silicate or phosphate [34-38]. Silicate electrolyte was known to produce more uniform porosity and morphology in MAO coating. On the other hand, phosphate electrolyte showed larger porosity with bigger crack size, which reduced the coating's corrosion resistance. Shen and coworkers [39] added sodium tetraborate ($Na_2B_4O_7 \cdot 10H_2O$) in electrolyte and found a reduction in the coating's surface porosity and a raise in its corrosion and wear resistance. Further addition of $K_2TiF_6$ in the previous electrolyte for the preparation of MAO on ZM21 magnesium alloy was able to promote the growth of oxide layer and the corrosion resistance as well [40]. Moreover, the increase in the concentration of silicate in the electrolyte drove the emergence of $Mg_2SiO_4$ from MgO and $SiO_2$ [41, 42]. Generally, the production of thicker and more compact coating was helpful in raising the surface hardness and corrosion resistance.

As for the current control in the MAO treatment, studies considering voltage level [44], pulse with different polarities and duty cycles [45], pulse frequency [46], and processing duration [47] have reported their influences on the coating's porosity, thickness, and corrosion property. Lower current density was found to produce more compact bonding between coating and magnesium substrate while its higher current counterpart prepared the coating with larger porosity and more cracks [43].

Regarding the biocompatibility of the prepared MAO coating, Xu and coworkers [48] conducted an in vitro test using embryonic bone cell of mouse (MC3T3-E1). They reported that although the MAO treatment could decrease the corrosion rate of magnesium alloy but no improvement on its biocompatibility was found. In a followed study by them, the prepared MAO specimen was implanted into a rat femur for an in vivo test. The result revealed the interaction between adsorbed protein and cell provided a good corrosion protection and alleviated the alloy's degradation.

According to the previous literature review, the use MAO treatment on AZ31B magnesium alloy and its biocompatibility study has not been published to the best knowledge of authors. Therefore, the potential of using AZ31B alloy as a biodegradable bone implant material was investigated in this study. A MAO treatment process employing pulsed DC current was attempted to control the corrosion rate and improve its biocompatibility. The corrosion behavior and mechanism of the MAO treated AZ31B alloy in the submersion of simulate body fluid (SBF) was explored in depth.

## 2. EXPERIMENTAL

In this study, pulsed DC current was adopted in the MAO treatment of an AZ31B magnesium alloy (Al 3-3.2%, Zn 0.8%, Mn 0.4%). The effects of different process parameters on the morphology, structure and corrosion performance of the derived oxide were investigated. The control on the corrosion rate of this magnesium alloy can be plausible by understanding its corrosion mechanism in SBF environment. Therefore, an X-ray diffractometer (SHIMADZU XRD-6000, HR-XRD, Japan) was employed in the crystallinity analysis of the prepared coating. Field-emission scanning electron microscope (JEOL JSM-7401F, FE-SEM, Japan) and transmission electron microscope (JEOL JEM-2100F, TEM, Japan) were used to examine the microstructural morphology. Both energy dispersive spectrometer (EDS) from the electron microscopes and X-ray photoelectron spectrometer (ULVAC-PHI, PHI 5000 VersaProbe, XPS, Japan) were used to perform the composition analysis on the surface and through-the-thickness of the coating, respectively. On the other hand, the hardness of the prepared coating was measured by using a microhardness tester (MVK-E36, MITUTOYO, Japan) with loading and duration set at 25 g and 10 s, respectively. The average and deviation of 5 measured points were reported in this study. More of specimen preparation and material characterization is explained in the following.

### *2.1 MAO Treatment*

The10×10 mm$^2$specimen was first cut from an AZ31B plate using a diamond saw cutter. Emery papers (#800 to #2000) were employed to polish and remove the oxide layer from the specimen's surface. The polished specimen was then rinsed and cleaned in an ultrasonic cleaner with alcohol and de-ionized water, followed by a 30-min drying at 80$^o$C. A further rinse with 10 wt% NaOH (Katayama Chemical Ind., Japan) solution was to degrease and remove possible debris. Finally, an activation using 10 wt% acetic acid ($CH_3COOH$) was performed before the MAO treatment. At this stage, the compositions of the AZ31B alloy were examined with an optical emission spectrometer (SHIMADZU pda-7000, Japan) to confirm its compliance with ASTM standard.

The electrolyte used in the MAO treatment contained 0.329M sodium silicate ($Na_2O{\bullet}2SiO_2{\bullet}nH_2O$, Showa Chemical, Japan), 0.75M NaOH and 0.272M sodium citrate ($C_6H_5Na_3O_7{\bullet}2H_2O$, Showa Chemical, Japan) in de-ionized water. The well mixed electrolyte was put in a stainless container which sat in a water bath controlled at 5$^o$C with a circulation cooling system. A magnetic stirrer was mounted under the stainless container to maintain uniform agitation of the electrolyte during the MAO treatment. Inside the electrolyte, the AZ31B specimen and the stainless container were connected to the anode and cathode of the electrical circuit, respectively. The electric power used was a pulsed DC current of 200-mA/cm$^2$ current density, 100-Hz frequency and 50% duty cycle [25]. Different MAO specimens were prepared with different time durations: 1, 5, 15, 30 and 40 min. After the MAO treatment, each specimen was cleaned and sonicated in a bath of alcohol and de-ionized water inside an ultrasonic cleaner.

### *2.2 In vitro Biocompatibility Test*

The simulated body fluid prepared in this study followed the solution compositions proposed by Kokubo and Takadama[49] which has similar ion concentration as human blood plasma. Table 1 presents the compositions of the SBF used in this study. In the preparation of SBF, the chemicals listed in Table

1 were added sequentially into 1000 ml of de-ionized water, and a hot plate with magnetic stirrer was employed to maintain uniform mixing at 37°C. The final pH of the SBF was tuned to 7.4 by using HCl. The specimen after MAO treatment was submerged in 30 ml of SBF which temperature was regulated at body temperature of 37°C using a circulating water bath. After every two days, the old SBF was drained from the glass beaker. Both the specimen and the beaker were cleaned with DI water and sonicated for 1 min. A new SBF was employed to rinse the specimen and the beaker to remove the possible residues in the cleaning step. Finally, 30-ml of new SBF was poured into the beaker and the specimen was submerged for further immersion test. The opening of the beaker was sealed with low permeability plastic wrap during immersion test. As mentioned before, 1, 3, 5, and 7 days of SBF immersion were performed. After the end of each immersion test, the specimen was rinsed and sonicated with ultrasonic cleaner for 1 min followed by a 24-hr baking in an oven at 45°C.

**Table 1.** The compositions of simulated body fluid (SBF) and its mixing sequence [49]

| Sequence | 1 | 2 | 3 | 4 | 5 | 6 | 7 |
|---|---|---|---|---|---|---|---|
| Chemical reagent | NaCl | $NaHCO_3$ | KCl | $K_2HPO_3$ | $MgCl_2•6H_2O$ | $CaCl_2$ | $Na_2SO_4$ |
| Weight (g) | 8.035 | 0.355 | 0.225 | 0.231 | 0.311 | 0.292 | 0.072 |

For the biocompatibility test, a control test on the pristine AZ31B was performed in addition to the experiment on the MAO treated specimen which had the best corrosion resistance among all MAO specimens prepared in different process parameters. The control specimen was polished sequentially to #2000 emery paper to remove the oxidized layer on surface. Then, the specimen was sterilized in 70% alcohol for 10 min. The sterilized specimen was moved to a 3.5 cm petri dish and air-blown for 10 min to remove the residual alcohol.

The mouse neuroblastoma cells (Neuro2a) with 40~50% were planted on a petri dish with additional 3 ml of culture fluid (900 ml Dulbecco's Modified Eagle Medium+10%FBS). The petri dish was then placed inside an incubator for 24 hr. After this 24-hr incubation period, the culture fluid in the petri dish was withdrawn to a 15 ml sterilized centrifuge tube and preserved at -20°C environment. The petri dish was rinsed with 1X PBS (Phosphate buffered saline) once and refilled with 1-ml new culture fluid to sustain the cell growth. Finally, optical microscope (OM) was employed to examine the cell development in the petri dish under the influence of coexisting magnesium alloy specimen.

### *2.3 Corrosion Characterization and Microstructural Analysis*

The specimen was first cold mounted using epoxy resin to expose a reactive area of 10×10 $mm^2$. Potentio-dynamic polarization measurement was performed by placing the specimen in SBF electrolyte and using a potentiostat (EG&G 263A, Princeton Applied Research, USA). A three-electrode configuration was adopted in this polarization measurement: saturated calomel electrode (SCE), platinum and specimen served as the reference electrode, counter electrode and working electrode, respectively. The range of voltage scan was from -2000 mV to 1000 mV in a scan rate of 1 mV/s and the corresponding corrosion potential ($E_{corr}$) and corrosion current ($I_{corr}$) were extracted from the measured polarization curve accordingly.

The X-ray diffraction measurement on the prepared coating was performed using copper target X-ray source with 0.15406-nm wavelength, 30-kV operation voltage, 30-mA operation current, $2^{o}$/min scanning rate. Moreover, the precipitation on specimen surface after the immersion treatment in SBF bath was examined through cross-sectional analysis. The binding energy of the elements near the coating's surface was measured by using X-ray photoelectron spectroscopy (XPS). After the removal of background signal using Shirley method, the binding energy spectra were de-convoluted into the contributions from different bonding. Subsequently, the element compositions and their chemical bonds of the SBF immersion treated specimen could be identified.

## 3. EXPERIMENTAL RESULTS

### *3.1 Microstructural Analyses and Hardness Measurements on the Treated Magnesium Alloy*

Table 2 presents the measured compositions of the AZ31B substrate used in this study. It is clearly seen that the substrate used in this study complied with the ASTM B90 specifications.

**Table 2.** Compositions of AZ31B magnesium alloy

| AZ31B | Al (wt%) | Mn (wt%) | Zn (wt%) | Mg (wt%) |
|---|---|---|---|---|
| ASTM B90 spec. | 2.50-3.50 | 0.20-1.00 | 0.60-1.40 | - |
| Substrate in this study | 2.59 | 0.27 | 0.97 | 96.17 |

The FE-SEM micrographs on the surface and cross-section of the specimens after MAO treatment of different durations, respectively are presented in Figure 1. Many micropores (ranging in sizes from 0.80 μm to 3.24 μm) and cracks are seen on the surface. The arcing observed on the surface during processing created the micropores and the rapid cooling of the fused oxide due to arcing caused the thermal microcracking [23, 50]. With the first increase in treatment duration, Figure 1 shows the growth of the oxide layer. However, after 30-min treatment, the thickness of oxide layer remained near 3 μm, with barely no growth at 40-min treatment. The partial detachment of the oxide layer from specimen surface during the sustained arcing in the processing could be the cause on the stagnation of oxide thickness growth [51].

Figure 2 shows the measured XRD spectra on the surface of specimen after MAO treatment of different durations. Similar diffraction patterns were obtained for specimens treated at different durations. The main constituents of the prepared coatings were found from the diffraction peaks as Mg (JCPDS 65-3365), MgO (JCPDS 65-0476), and $MgSiO_3$ (JCPDS 39-0048). The diffraction peaks of Mg should derive from the substrate while those of MgO should come from the product of the micro arcing reaction. The emergence of $MgSiO_3$ could be due to the reaction of $SiO_2$ and MgO, in which $SiO_2$ was derived from the hydrolysis of $NaSiO_3$ in the electrolyte. The compositions of the prepared coatings were further examined by FESEM-EDS measurement and the results are presented in Table 3.

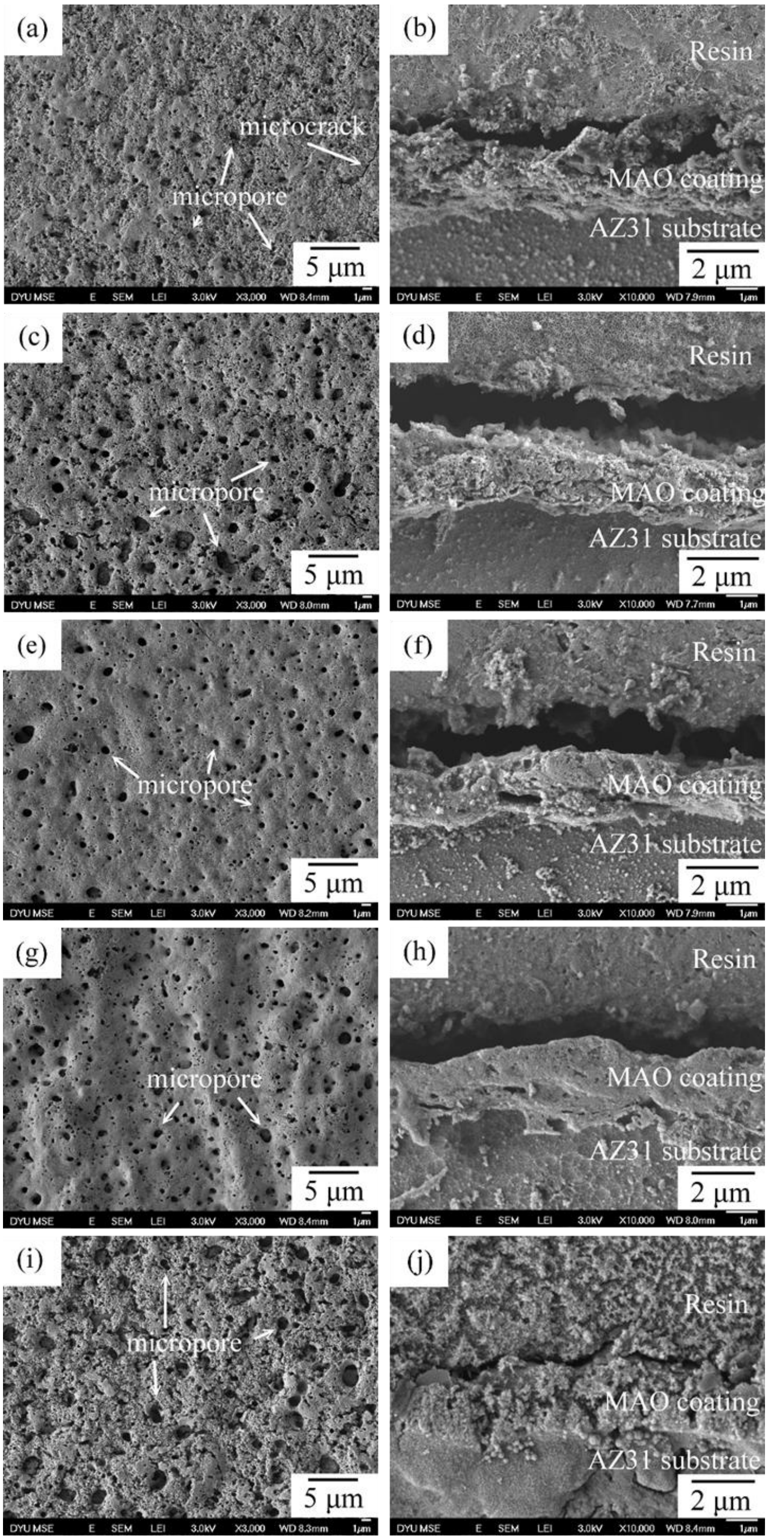

**Figure 1.** The FE-SEM micrographs on the surface and cross-section of specimens after MAO treatment of different durations, respectively: (a, b) 1 min, (c, d) 5 min, (e, f) 15 min, (g, h) 30 min, (i, j) 40 min

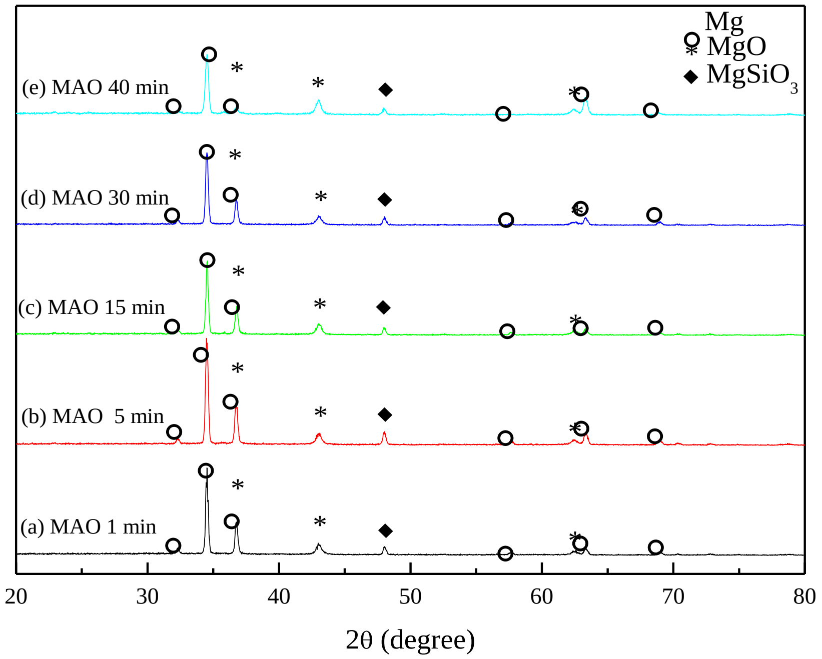

**Figure 2.** The measured XRD spectra on surface of the specimens after MAO treatment of different durations, respectively: (a) 1 min, (b) 5 min, (c) 15 min, (d) 30 min, (e) 40 min

**Table 3.** The compositions of the prepared MAO coatings measured by FESEM-EDS analysis

| Element / Duration of MAO processing | Mg (at%) | Si (at%) | Al (at%) | Zn (at%) | O (at%) |
|---|---|---|---|---|---|
| 1 min | 50.33 | 4.39 | 1.12 | 0.31 | 47.85 |
| 5 min | 39.02 | 5.71 | 1.30 | 0.27 | 53.70 |
| 15 min | 35.32 | 7.38 | 0.68 | 0.21 | 61.40 |
| 30 min | 33.66 | 7.81 | 0.78 | 0.41 | 57.35 |
| 40 min | 32.75 | 8.71 | 0.65 | 0.09 | 56.56 |

It is seen that except the coating with 1 min processing duration revealed contents with higher Mg and lower O, the compositions of O, Mg, Al, Si and Zn for other processing durations showed little variations [42].

**Table 4.** The measured surface hardness of the MAO coatings prepared with different durations

| Duration of MAO processing | AZ31B | 1 min | 5 min | 15 min | 30 min | 40 min |
|---|---|---|---|---|---|---|
| Hardness (HV) | 63.18± 1.65 | 92.94± 7.69 | 93.41± 4.51 | 101.34± 4.73 | 103.67± 2.38 | 117.39± 0.77 |

Table 4 presents the measured surface hardness of the MAO coatings prepared with different processing durations. It is clearly seen that the hardness increased with processing duration and its magnitude increased from 63.18 HV of the substrate to 117.39 HV of the 40-min treated coating. The raise in surface hardness after the MAO treatment denotes the wear resistance of the Mg alloy can be improved accordingly.

### *3.2 Corrosion Polarization Characteristics*

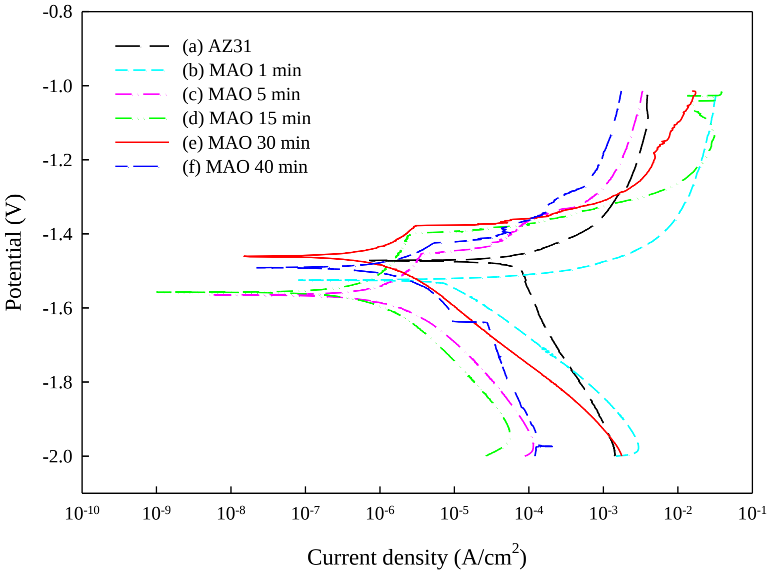

**Figure 3.** Polarization curves of specimens after different durations of MAO treatment: (a) 0 min, (b) 1 min, (c) 5 min, (d) 15 min, (e) 30 min, (f) 40 min

Figure 3 presents the measured polarization curves of the specimens after different durations of MAO treatment. The corresponding corrosion potentials ($E_{corr}$) and corrosion current densities ($i_{corr}$) were distilled from these polarization curves and are listed in Table 5.

**Table 5.** Corrosion potential and corrosion current of the specimens after different durations of MAO treatment.

| Duration of MAO processing | AZ31B | 1 min | 5 min | 15 min | 30 min | 40 min |
|---|---|---|---|---|---|---|
| $E_{corr}$ (V) | -1.47 | -1.52 | -1.56 | -1.55 | -1.46 | -1.48 |
| $i_{corr}$ (A/cm$^2$) | $2.02\times10^{-4}$ | $8.18\times10^{-6}$ | $2.74\times10^{-6}$ | $2.08\times10^{-6}$ | $1.26\times10^{-6}$ | $2.32\times10^{-6}$ |

The measured $E_{corr}$ and $i_{corr}$ for the substrate were -1.47 V and $2.02\times10^{-4}$ A/cm$^2$, respectively. With the MAO treatment, the $E_{corr}$ showed slight change with the treatment duration. However, the $i_{corr}$ decreased to $1.26\times10^{-6}$ A/cm$^2$ after 30 min of MAO treatment. The results demonstrated that in SBF electrolyte the pristine AZ31B had lowest $E_{corr}$ and highest $i_{corr}$, and subsequently, the most severe corrosion rate. Among the MAO-treated specimens, the one with 30-min processing duration revealed the lowest $i_{corr}$ and the highest $E_{corr}$. The MAO-treatment significantly improved the corrosion resistance of AZ31B [24, 26].

The growth in oxide thickness and the densification of the porous structure after longer treatment duration, as seen in Fig. 1(e, f), raised its corrosion resistance. But at 40-min MAO treatment, the breakaway of oxide from the specimen surface roughened the surface and lowered the corrosion resistance consequently.

### *3.3 Biocompatibility and Cytotoxicity of the Prepared Coating*

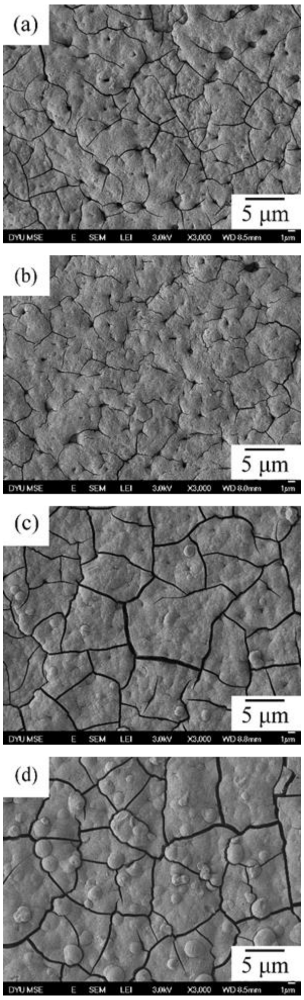

**Figure 4.** The FE-SEM micrographs of the specimen after immersion in SBF for different durations: (a) 1 day, (b) 3 days, (c) 5 days, (d) 7 days.

Since the MAO treated specimen had best corrosion resistance at 30-min processing duration, only this specimen was adopted in the biocompatibility test in SBF bath. The FE-SEM micrographs of the specimen after immersion in SBF for 1, 3, 5 and 7 days, respectively, were shown in Figure 4. It is clearly seen that with the increase in the duration of immersion treatment the number of micropores decreased. The surface was coated by a new layer, which developed contraction cracks upon dehydration of the specimen. The composition and structure of this new layer was examined by using HR-XRD diffractometer. The measured diffraction spectra presented in Figure 5 show an apatite peak at 31.8° in addition to other peaks associated with Mg, MgO and $MgSiO_3$ reported previously in Figure 2. Moreover, this apatite peak grew in magnitude as the duration of immersion increased. Therefore, the surface layer observed in Figure 4 was confirmed as the apatite formed during the immersion of SBF.

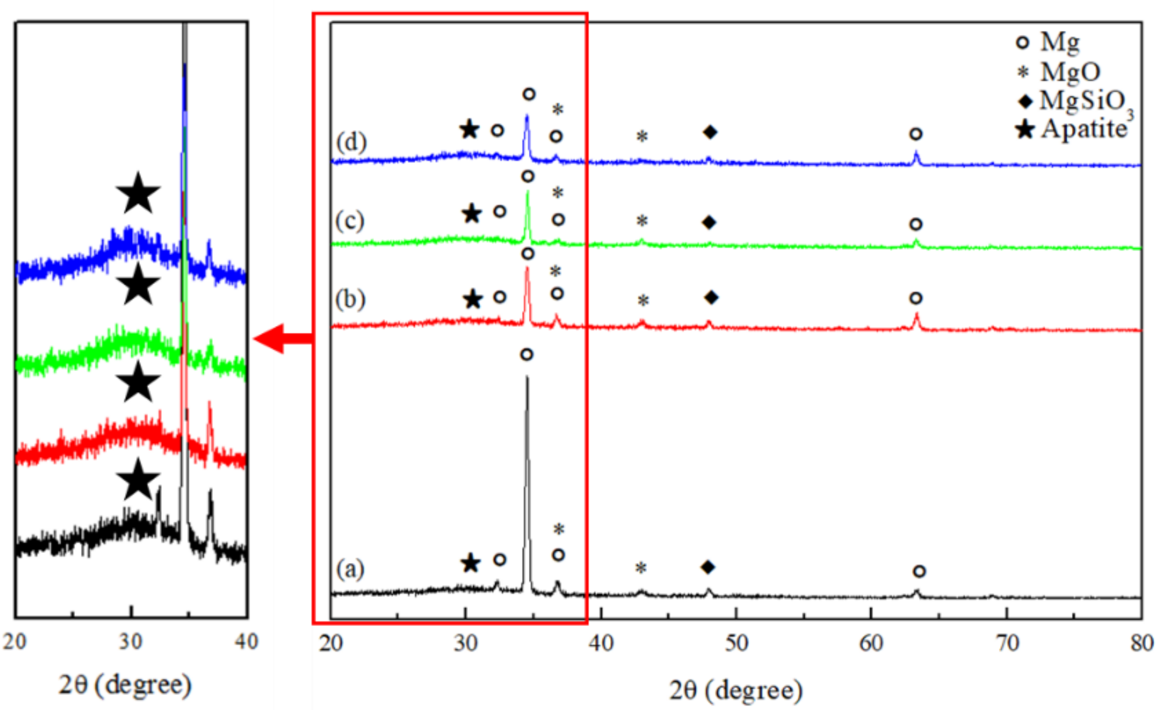

**Figure 5.** The HR-XRD diffraction spectra of MAO-treated AZ31B specimen immersed in SBF bath for different time durations: (a) 1 day, (b) 3 days, (c) 5 days, (d) 7 days

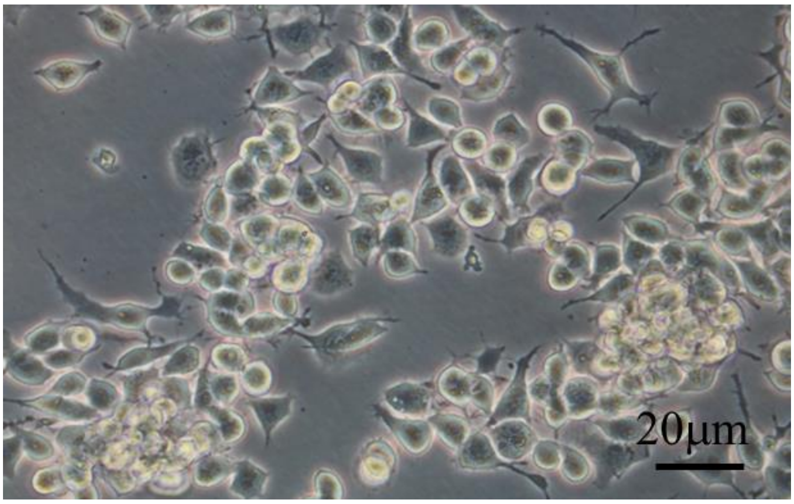

**Figure 6.** The optical microscope of mouse neuroblastoma cells Neuro2a cultured MAO-treated AZ31B specimen for 24 hr.

The biocompatibility of the MAO treated specimen was further checked with cell culture. Figure 6 shows the optical microscope of the planted 40~50% Neuro2a cells in the specimen after a 24-hr culture. Obviously, the Neuro2a cells survived very well and developed axons during this culture. Thus, the MAO treated AZ31B alloy was considered biocompatible with neuroblastoma cells.

## 4. DISCUSSION

### *4.1 Microstructure of the MAO Coating*

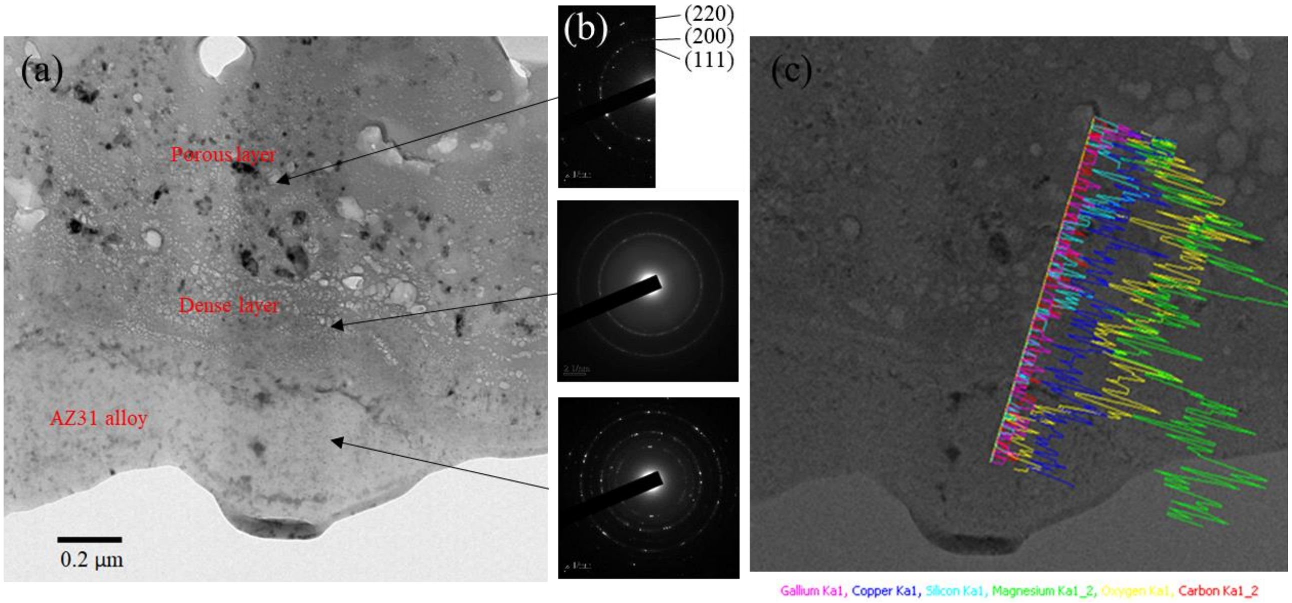

**Figure 7.** Cross-sectional TEM analyses on the coating of the 30-min MAO treated specimen: (a) micrograph, (b) selected area electron diffraction (SAED) patterns, (c) compositional line scan.

Figure 7(a, b) shows the TEM micrographs on the cross section of the 30-min MAO treated specimen. Three-layer structure consisting of porous layer, dense layer and substrate can be easily seen in the micrographs. The size of the pores in the porous layer ranged from micrometers to nanometers. During micro-arc-oxidization process, the generated oxide continuously melted and solidified which provided the driving force for the grain nucleation and growth. Thus, there were large-sized grains found in the porous layer. Those nanosized grains were mostly made of MgO and oriented preferably in (111), (200) and (220) directions detected from the SAED measurement. In between the porous layer and substrate, there existed a 200 nm to 500 nm thick dense layer. This dense layer was found to be an amorphous MgO ceramic. The corresponding line scan on the compositions indicated in Figure 7(c) revealed lower Mg content in the dense layer. The microstructure found in this study was similar to that reported by Khaselev et al. [52] in the MAO-treated Mg-Al alloy.

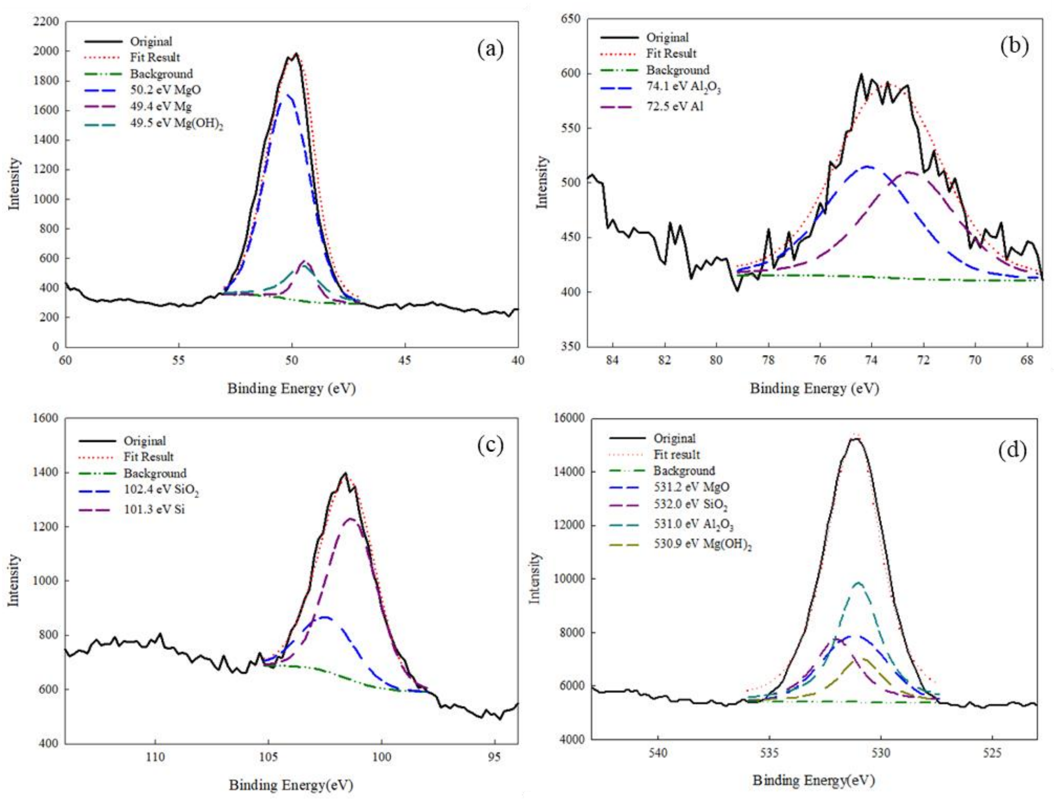

**Figure 8.** Results of the XPS analysis on the coating of the 30-min treated MAO specimen: (a) Mg2p, (b) Al2p, (c)Si2p, (d) O1s

**Table 6.** The analyzed results from XPS measurement and the associated reference binding energies from NIST USA.

| Element | Spectral line | Formula | Binding energy (eV) | |
|---|---|---|---|---|
| | | | NIST* | Experimental on the surface |
| Mg | 2p | Mg | 49.4 | 49.4 |
| Mg | 2p | MgO | 50.2 | 50.2 |
| Mg | 2p | $Mg(OH)_2$ | 49.5 | 49.5 |
| Al | 2p | Al | 72.5 | 72.5 |
| Al | 2p | $Al_2O_3$ | 74.1 | 74.1 |
| Si | 2p | Si | 101.3 | 101.3 |
| Si | 2p | $SiO_2$ | 102.4 | 102.4 |
| Ca | 2p3/2 | $Ca_{10}(PO_4)_6(OH)_2$ | 347.7 | 347.7 |
| P | 2p3/2 | $Ca_{10}(PO_4)_6(OH)_2$ | 133.0 | 133.0 |
| O | 1s | MgO | 531.2 | 531.2 |
| O | 1s | $Mg(OH)_2$ | 530.9 | 530.9 |
| O | 1s | $Al_2O_3$ | 531.0 | 531.0 |
| O | 1s | $SiO_2$ | 532.0 | 532.0 |
| O | 1s | $Ca_{10}(PO_4)_6(OH)_2$ | 531.8[44] | 531.8 |

*Source of reference: XPS database from NIST USA, http://srdata.nist.gov/xps/.

The result of the XPS analysis for the same specimen is shown in Figure 8. It can be confirmed that the MAO coating mainly composed of Mg, Al, Si and O elements. Figure 8(a) is the Mg2p peak which consists of binding energy of 49.4 eV for Mg and binding energy of 50.2 eV for MgO. Figure 8(b) is the Al2p peak which consists of binding energy of 74.1 eV for $Al_2O_3$ and binding energy of 72.5 eV for Al. Figure 8(c) is the Si2p peak which consists of binding energy of 102.4 eV for $SiO_2$ and binding energy of 101.3 eV for Si. Figure 8(d) presents the O1s peak which consists of contribution from 4 constituents: 531.2 eV for MgO, 532.0 eV for $SiO_2$, 531.0 eV for $Al_2O_3$, and 530.9 eV for $Mg(OH)_2$. In summary, Table 6 lists the measurement results and the sources of the reference binding energies.

These results confirmed the MAO coating contained following elements and compounds: Mg, MgO, $Al_2O_3$, Al, $SiO_2$ and Si.

### *4.2 Microstructure of the SBF-Immersed MAO Coating*

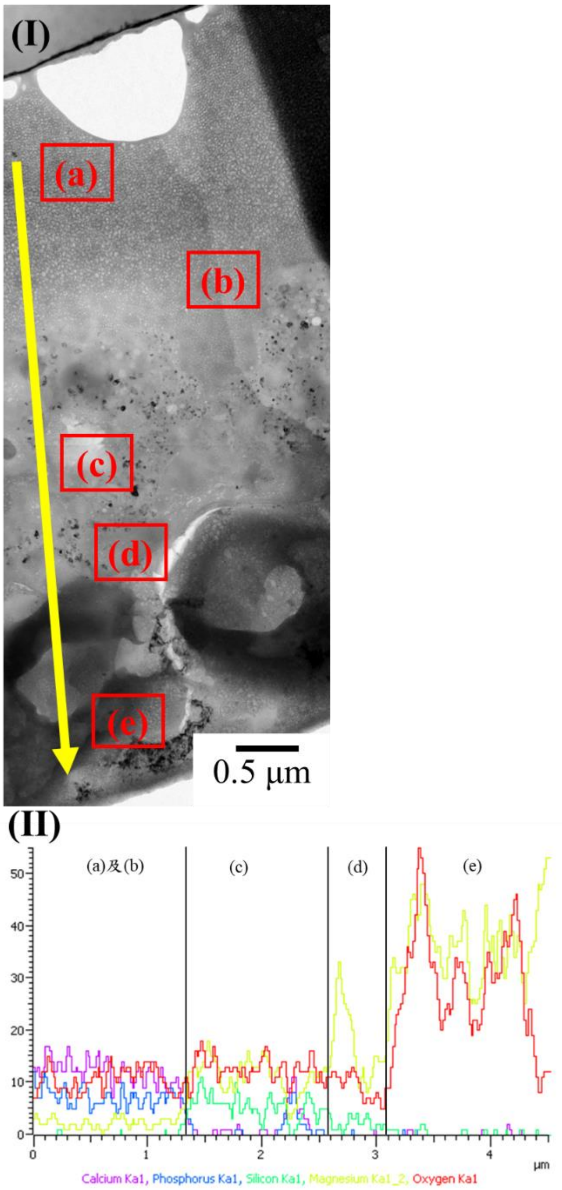

**Figure 9.** The TEM examination on the cross section of the 30-min treated MAO coating after 7-day immersion in SBF bath: (I)TEM micrograph, (II) composition line scan

The TEM examination result on the cross section of the 30-min treated MAO coating after 7-day immersion in SBF bath is presented in Figure 9. In Figure 9(I), (a, b) denote the precipitation layer while (c, d) the porous layer. By referring to Figure 7(a) for the specimen without immersion treatment, the porosity in the porous layer of Figure 9(Ic) increased not only in number but also in size of the pores. This observation revealed SBF could corrode the MAO coating and proceeded in pitting corrosion. Several coarse MgO or Mg grains were found in the previous porous layer of MAO-treated coating. More distinctly, the previously existed pores disappeared. Those micropores should be filled with the apatite precipitation product from reaction between MAO and SBF, which was substantiated by the detection of P and Ca elements in the line scan results of Figure 9(II). Therefore, the immersion of MAO coating into the SBF bath induced the corrosion reaction of MgO with the solution. Gu and coworkers [53] proposed this corrosion was controlled by dense layer, porosity and MAO layer thickness. The corrosion on the surface of the MAO coating could effectively alleviated the possible corrosion reaction of the substrate. By comparing the results shown in Figure 7(a) and Figure 9(c, d), it is realized that as the SBF entered MAO coating, the small grains of magnesium alloy would be corroded and generate porosity in the porous layer. The corrosion enlarged during the corrosion process and facilitated the penetration of SBF into the dense layer. The subsequently corrosion reaction turned the dense layer into amorphous ceramic structure. The composition line scan result in the porous layer, Figure 9(II), revealed the drop of Mg content from 35 wt% to 12 wt% while the Mg content remained nearly unchanged in the dense layer. Moreover, the raise of O content near the substrate from 2 wt% to 13 wt% indicated the corrosion reaction in the substrate, as seen in Figure 9(c, e). Therefore, it is understood that as soon as the SBF penetrated through the MAO layer and reached the substrate, quick corrosion reaction could start [41].

**Table 7.** The TEM-EDS measured compositions of the 30-min MAO treated coating after immersion in SBF bath for 7 days. Location is as indicated in Figure 9.

| Element (at%) / Location | O | Mg | P | Ca | Si | Al |
|---|---|---|---|---|---|---|
| (a) | 61.69 | 5.74 | 12.86 | 19.71 | - | - |
| (b) | 69.74 | 7.74 | 10.22 | 12.29 | - | - |
| (c) | 64.03 | 25.47 | 2.43 | 3.1 | 4.96 | |
| (d) | 61.79 | 34.88 | - | - | 1.8 | 1.53 |
| (e) | 62.41 | 37.59 | - | - | - | - |

Table 7 lists the TEM-EDS measured compositions of the 30-min MAO treated coating after immersion in SBF bath for 7 days. The location in the table is as indicated correspondingly in Figure 9(I). The precipitation layer, location (a) and (b), mainly composed of O, Ca and P. Some Mg but no trace of Si was detected. Thus, this was the precipitation layer of apatite. The porous layer, location (c), contained Mg, O, Ca, P and Si elements. The detection of lower amount of P and Ca denoted the start of corrosion reaction with SBF to produce apatite. No trace of Ca and P were found at location (d). It seemed that SBF did not reach this depth. Finally, Only Mg and O were detected dominantly at location (e). This dense layer was likely MgO. General speaking, the formation apatite on the surface of the MAO coating can repair the porosity and cracking. Subsequently, the corrosion rate of the treated magnesium alloy can be alleviated [35].

### *4.3 The XPS and Molar Ca/P Ratio Analyses on the SBF-Immersed MAO Coating*

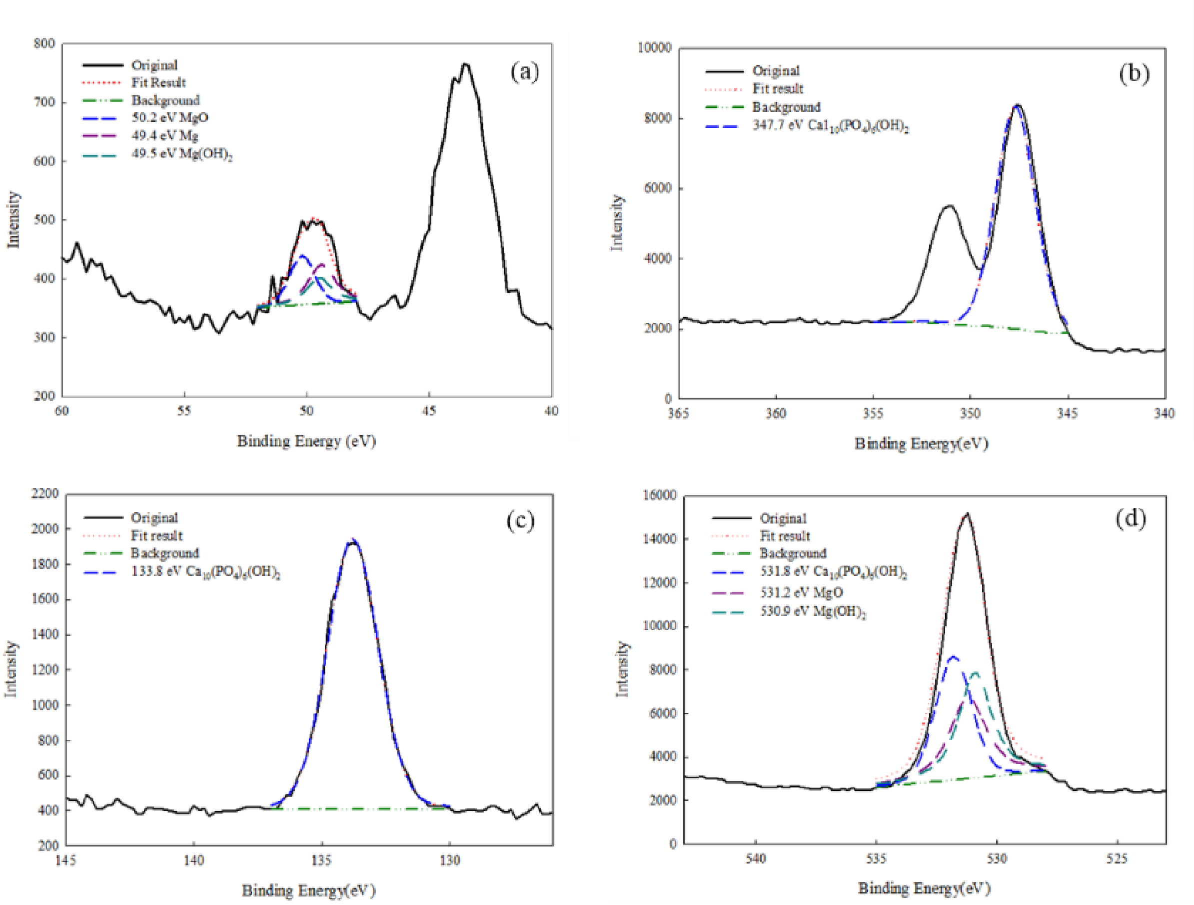

**Figure 10.** The XPS analysis on the surface of MAO coating after 7-day immersion in SBF bath: (a)Mg2p, (b) Ca2p, (c) P2p, (d) O1s

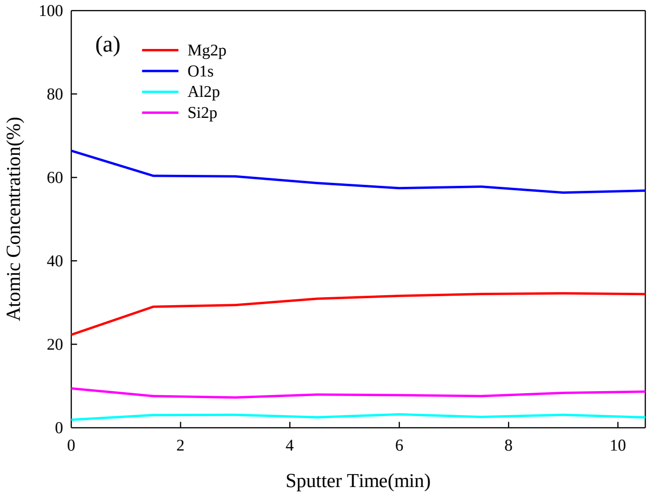

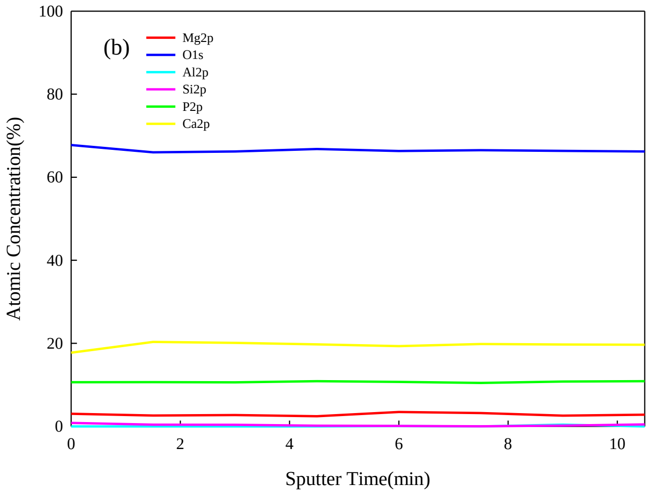

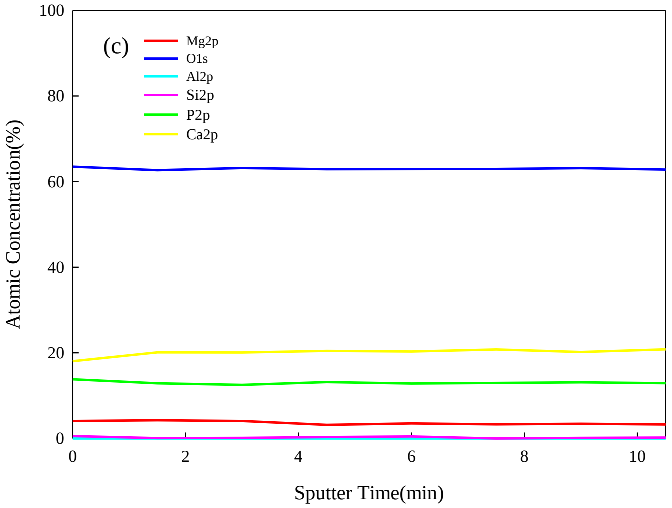

**Figure 11.** The through-the-thickness XPS analysis on three different coatings: (a) 30-min MAO treated coating, (b) the MAO coating after 1-day SBF immersion, (c) The MAO coating after 7-day SBF immersion.

Figure 10 presents the XPS analysis results of the surface of the MAO coating after 7-day immersion in SBF bath. The results revealed the existence of Mg, O, Ca, P, Si and Al in the coating. Figure 10(a) is the Mg2p peak which consists of binding energy of 49.4 eV for Mg, binding energy of 50.2 eV for MgO, and binding energy of 49.5 eV for $Mg(OH)_2$. Figure 10(b) is the Ca2p3/2 peak which consists of binding energy of 347.7 eV for $Ca_{10}(PO_4)_6(OH)_2$ only. Figure 10(c) is the P2p3/2 peak which also consists of binding energy of 133.8 eV for $Ca_{10}(PO_4)_6(OH)_2$ [44]. Figure 10(d) presents the O1s peak which consists of contribution from 3 constituents: 531.8 eV for $Ca_{10}(PO_4)_6(OH)_2$, 531.2 eV for MgO, and 530.9 eV for $Mg(OH)_2$. From these results, it can be confirmed that the surface of the SBF-immersed MAO coating contained Mg, MgO, $Mg(OH)_2$, and $Ca_{10}(PO_4)_6(OH)_2$ constituents. In order to examine the composition variation through the coating's thickness, an $Ar^+$ ablation with 2-keV voltage over a 2×2 mm area was employed with controlled etching duration. One minute sputtering interval was adopted in this through-the-thickness measurement. For reference, this ablation setting can etch a $SiO_2$ substrate in a rate of 13.73 nm/min. Figure 11 presents the through-the-thickness XPS analysis results on three different coatings: the pristine MAO coating, and the MAO coatings after 1-day and 7-day immersion in SBF bath, respectively. Figure 11(a) shows the constituents of pristine MAO coating are simply Mg, Si, Al, and O. However, after 1-day immersion in SBF bath, the apatite containing Ca and P prevailed within the depth of measurement, as seen in Figure 11(b). Nevertheless, increasing the duration of immersion to 7 days did not have significant effect on the composition content of apatite.

Calcium phosphate is the main ingredient in human bone and teeth. As an engineering ceramic, hydroxyapatite (HAp: $Ca_{10}(PO_4)_6(OH)_2$) has excellent bioactivity, biocompatibility, osteoconductivity, similar chemical and crystalline structure with apatite in human bone. The Ca/P molar ratio is 1.67 in solid HAp while 1.50-1.67 in amorphous HAp [47, 54, 55]. In order to verify the structure of the apatite prepared in this study, its Ca/P ratio was also examined. From the EDS measurement listed in Table 7, the Ca/P ratio for the specimen after 7-day immersion in SBD bath was 1.53. On the other hand, from the XPS measured results shown in Figure 11(b, c), the Ca/P ratios for the 1-day and 7-day immersion were 1.67 and 1.54, respectively. From these results, the Ca/P ratio for the precipitated apatite prepared in this study was fairly close to the reported range of 1.50-1.67 for amorphous HAp.

## 5. CONCLUSION

In this study, the MAO coating prepared on the AZ31B magnesium alloy was found to have inner dense layer and outer porous layer grown on the substrate via SEM and TEM examinations. The population of surface micropores and the coating thickness increased with the MAO-treated duration. This coating mainly consisted of Mg, MgO and $MgSiO_3$ and effectively raised the hardness to 117.39 HV from 63.18 HV of the substrate. Thus, the increase in wear resistance of the Ma alloy can be expected. From the measured polarization curves, the specimen with 30-min MAO treatment showed the least corrosion current. Longer treatment duration did not further enhance the corrosion resistance due to flaking of oxide in the MAO processing. The immersion of MAO-treated specimen in SBF bath showed a uniform corrosion and an emergence of precipitated apatite over the surface. Underneath the precipitated apatite, local pitting near the substrate interface appeared. The penetration of SBF through the porous layer further corroded the substrate. This mechanism demonstrated the continuous degradation of the substrate in SBF immersion. The through-the-thickness XPS analysis revealed that the duration of SBF immersion from 1 day to 7 days did not change the contents of Ca and P which were related the existence of apatite. One-day immersion in SBF bath was able to obtain the required thickness of apatite. Finally, the culture of planted mouse neuroblastoma cells (Neuro2a) with MAO-treated specimen in SBF demonstrated the well survival and even axon development of the cells.

ACKNOWLEDGEMENT
The authors thank the financial supports from University System of Taipei Joint Research Program, USTP-NTUT-NTOU-109-04.

## References

1. M.P. Staiger, A.M. Pietak, J. Huadmai, G. Dias, *Biomaterials*, 27 (2006) 1728.

2. F. Witte, J. Fischer, J. Nellesen, H.A. Crostack, V. Kaese, A. Pisch, F. Beckmann, H. Windhagen, *Biomaterials*, 27 (2006) 1013.
3. R. Zeng, W. Dietzel, F. Witte, N. Hort, C. Blawert, *Adv. Mater.*, 10 (2008) B3.
4. A. Lambotte, *Presse Med Belge*, 17 (1909) 321.
5. B. Heublein, R. Rohde, V. Kaese, M. Niemeyer, W. Hartung, A. Haverich, *Heart*, 89 (2003) 651.
6. F. Witte, V. Kaese, H. Haferkamp, E. Switzer, A. Meyer-Lindenberg, C.J. Wirth, H. Windhagen, *Biomaterials*, 26 (2005) 3557.
7. F. Witte, F. Feyerabend, P. Maier, J. Fischer, M. Störmer, C. Blawert, W. Dietzel, N. Hort, *Biomaterials*, 28 (2007) 2163.
8. D. Williams, *Medical Device Technology*, 17 (2006) 9-10.
9. P. Helmecke, M. Ezechieli, C. Becher, J. Köhler, B. Denkena, *Biomed. Tech.*, (2013) 58.
10. H. Windhagen, K. Radtke, A. Weizbauer, J. Diekmann, Y. Noll, U. Kreimeyer, R. Schavan, C. Stukenborg-Colsman and H. Waizy, *Biomed. Eng. Online*, 12 (2013) 62.
11. J.W. Lee, H.S. Han, K.J. Han, J. Park, H. Jeon, M.R. Ok, H.K. Seok, J.P. Ahn, K.E. Lee, D.H. Lee, S.J. Yang, S.Y. Cho, P.R. Cha, H. Kwon, T.H. Nam, J.H. Han, H.J. Rho, K.S. Lee, Y.C. Kim, D. Mantovani. *Proc. Natl. Acad. Sci. U. S. A.*, 113 (2016) 716.
12. Y. Gu, X. Cai, Y. Guo, C. Ning, *Mater. Des.*, 43 (2013) 542.
13. W.D. Mueller, M.L. Nascimento, M.F. Lorenzo de Mele, *Acta Biomater.*, 6 (2010) 1749.
14. Ya. Unigovski, A. Eliezer, E. Abramov, Y. Snir, E.M. Gutman, *Mater. Sci. Eng.* A, 360 (2003) 132.
15. X. Yan, M.C. Zhao, Y. Yang, L. Tan, Y.C. Zhao, D.F. Yin, K. Yang, A. Atrens, *Corros. Sci.*, 156 (2019) 125.
16. Y.F. Zheng, X.N. Gu, F. Witte, *Mater. Sci. Eng. R. Rep.*, 77 (2014) 1.
17. M. Erinc, W.H. Sillekens, R.G.T.M. Mannens, R.J. Werkhoven, *Magnesium Technology*, 15 (2009) 209.
18. M. Ali, M.A. Hussein, N. Al-Aqeeli, *J. Alloys Compd.*, 792 (2019) 1162.
19. J. Chen, L. Tan, X. Yu, I.P. Etim, M. Ibrahim, K. Yang, *J. Mech. Behav. Biomed. Mater.*, 87 (2018) 68.
20. H. Liu, F. Cao, G.L. Song, D. Zheng, Z. Shi, M.S. Dargusch, *J. Mater. Sci. Technol.*, 35 (2019) 2003.
21. H. Hornberger, S. Virtanen, A.R. Boccaccini, *Acta Biomater*, 8 (2012) 2442.
22. L. Xu, F. Pan, G. Yu, L. Yang, E. Zhang, K. Yang, *Biomaterials*, 30 (2009) 1512.
23. G. Barati Darband, M. Aliofkhazraei, P. Hamghalam, N. Valizade, *J. Magnes. Alloy.*, 5 (2017) 74.
24. Y. Pan, S. He, D. Wang, D. Huang, T. Zheng, S. Wang, P. Dong, C. Chen, *Mater. Sci. Eng.* C, 47 (2015) 85.
25. A. L. Yerokhin, A. Shatrov, V. Samsonov, P. Shashkov, A. Leyland, A. Matthews, *Surf. Coat. Technol.*, 182 (2004) 78.
26. S.Y. Jian, J.L. Lee, H.B. Lee, H.H. Sheu, M.H. Lin, Y.T. Shih, C.A. Chen, J.K. Chang, M.D. Ger, *Int. J. Electrochem. Sci.*, 13 (2018) 5709.
27. T.S.N. Sankara Narayanan, I. S. Park, M.H. Lee, *Prog. Mater. Sci.*, 60 (2014) 1.
28. M. Toorani, M Aliofkhazraei, R. Naderi, *J. Alloys Compd.*, 785 (2019) 669.
29. C.Y. Li, X.L. Fan, R.C. Zeng, L.Y. Cui, S.Q. Li, F. Zheng, Q.K. He, M. Bobby Kannan, H.W. Jiang, D.C. Chen, S.K. Guan, *J. Mater. Sci. Technol.*, 35 (2019) 1088.
30. X. Zheng, Q. Liu, H. Ma, S. Das, Y. Gu, L. Zhang, *Surf. Coat. Technol.*, 347 (2018) 286.
31. B. Mingo, R. Arrabal, M. Mohedano, Y. Llamazares, E. Matykina, A. Yerokhin, A. Pardo, *Appl. Surf. Sci.*, 433 (2018) 653.
32. Y. Wang, X. Wang, T. Zhang, K. Wu, F. Wang, *J. Mater. Sci. Technol.*, 29 (2013) 1129.
33. L. R. Krishna, G. Poshal, A. Jyothirmayi, G. Sundararajan, *Mater. Des.*, 77 (2015) 6.
34. R.F. Zhang, S.F. Zhang, J.H. Xiang, L.H. Zhang, Y.Q. Zhang, S.B. Guo, *Surf. Coat. Technol.*, 206 (2012) 5072.

35. W. Yang, D. Xu, X. Yao, J. Wang, J. Chen, *J. Alloys Compd*., 745 (2018) 609.
36. Z. Li, Q. Yu, C. Zhang, Y. Liu, J. Liang, D. Wang, F. Zhou, *Surf. Coat. Technol*., 357 (2019) 515.
37. C.E. Barchiche, E. Rocca, C. Juers, J. Hazan, J. Steinmetz, *Electrochim. Acta*, 53 (2007) 417.
38. Y. Mori, A. Koshi, J. Liao, H. Ahoh, S. Ono, *Corros. Sci*., 88 (2014) 254.
39. M.J. Shen, X.J. Wang, M.F. Zhang, *Appl. Surf. Sci*., 259 (2012) 362.
40. D. Sreekanth, N. Rameshbabu, K. Venkateswarlu, Ch. Subrahmanyam, L. Rama Krishna, K. Prasad Rao, *Surf. Coat. Technol*., 222 (2013) 31.
41. B. Salami, A. Afshar, A. Mazaheri, *J. Magnes. Alloy*, 2 (2014) 72.
42. S. Levent Aktuğ, SalihDurdu, I. Kutbay, M. Usta, *Ceram. Int*., 42 (2016) 1246.
43. P. Bala Srinivasan, J. Liang, C. Blawert, M. Störmer, W. Dietzel, *Appl. Surf. Sci*., 255 (2009) 4212.
44. Y. Li, F. Lu, H. Li, W. Zhu, H. Pan, G. Tan, Y. Lao, C. Ning, G. Ni, *Prog. Nat. Sci*., 24 (2014) 516-522.
45. S.J. Lee, L.H.T. Do, J.L. Lee, C.Y. Chen, P.C. Peng, *Int. J. Electrochem. Sci*., 13 (2018) 2705-2717.
46. X. Song, J. Lu, X. Yin, J. Jiang, J. Wang, *J. Magnes. Alloy*, 1 (2013) 318.
47. Y. Gu, S. Bandopadhyay, C.F. Chen, Y. Guo, C. Ning, *J. Alloys Compd*., 543 (2012) 109.
48. H. Xu, T. Hu, M. Wang, Y. Zheng, H. Qin, H. Cao, Z. An, *Arab. J. Chem*., 20 (2018) 2795.
49. T. Kokubo, H. Takadama, *Biomaterials*, 27 (2006) 2907-2915.
50. H. Duan, C. Yan, F. Wang, *Electrochim. Acta*, 52 (2007) 3785.
51. M.M.S. Al Bosta, K.J. Ma and H.H. Chien, *Infrared. Phys. Technol*., 60 (2013) 323.
52. O. Khaselev, D. Weiss, J. Yahalom, *Corros. Sci*., 43 (2001) 1295.
53. Y. Gu, C. f. Chen, S. Bandopadhyay, C. Ning, Y. Zhang, Y. Guo, *Appl. Surf. Sci*., 258 (2012) 6116.
54. M.T. Carayon, J.L. Lacout, *J. Solid State Chem*., 172 (2003) 339.
55. E. Boanini, M. Gazzano, A. Bigi, *Acta Biomater*., 6 (2010) 1882.